RSC Advances

PAPER

View Article Online
View Journal | View Issue

Cite this: *RSC Adv.*, 2019, **9**, 18874

Folic acid-conjugated gold nanorod@polypyrrole@Fe_3O_4 nanocomposites for targeted MR/CT/PA multimodal imaging and chemo-photothermal therapy†

Wei Cao,‡[ab] Xuandong Wang,‡[ab] Liang Song,[ab] Peiyuan Wang,[ab] Xuemei Hou,[ab] Huicong Zhang,[ab] Xiangdong Tian,[ab] Xiaolong Liu *[abc] and Yun Zhang *[ab]

Integrating multimodal bioimaging and different therapies into one nanoplatform is a promising strategy for biomedical applications, but remains a great challenge. Herein, we have synthesized a biocompatible folic acid (FA) functionalized gold nanorod@polypyrrole@Fe_3O_4 (GNR@PPy@Fe_3O_4-FA) nanocomposite through a facile method. The conjugated FA has endowed the nanocomposite with the ability to recognize targeted cancer cells. Importantly, the nanocomposite has been successfully utilized for magnetic resonance (MR), computed tomography (CT) and photoacoustic (PA) multimodal imaging. Moreover, the GNR@PPy@Fe_3O_4-DOX nanocomposite shows pH-responsive chemotherapy and enables the integration of photothermal therapy and chemotherapy to achieve superior antitumor efficacy. The GNR@PPy@Fe_3O_4-DOX nanocomposites have a drug release of 23.64%, and the photothermal efficiency of the GNR@PPy@Fe_3O_4 nanocomposites reaches 51.46%. Cell viability decreases to 15.83% and 16.47% because of the combination of chemo-photothermal therapy effects. Moreover, the GNR@PPy@Fe_3O_4-DOX-FA nanocomposite could target cancer cells *via* folic acid and under a magnetic field. The *in vivo* multimodal imaging and chemo-photothermal therapy effects showed that the GNR@PPy@Fe_3O_4-DOX-FA nanocomposites are a good contrast and theranostic agent. Thus, this multifunctional nanocomposite could be a promising theranostic platform for cancer diagnosis and therapy.

Received 22nd January 2019
Accepted 26th May 2019

DOI: 10.1039/c9ra00541b

rsc.li/rsc-advances

Introduction

Cancer has seriously threatened human health, and traditional chemotherapy is still one of the most common methods used for cancer therapy.[1–3] However, chemotherapy drugs are often considered to easily cause systemic side effects and induce complications to patients when killing cancer cells, because of the lack of specificity for cancer cells and their serious toxicity to normal cells and tissues.[4,5] Thus, the development of nanobiotechnology and photothermal therapy (PTT), which is able to kill cancer cells through converting absorbed near-infrared (NIR) light into localized heat by using NIR-absorbing agents, has been explored for cancer therapy.[6–8] Compared with traditional clinical therapies, such as surgery, chemotherapy or radiotherapy, PTT is a minimally invasive, highly selective therapy technique with low side effects.[9] Therefore, various materials with strong absorbance in the NIR region have drawn much attention, such as gold-based nanostructures,[10–13] graphene oxide,[14–16] CuS/Se related materials[17–19] and carbon nanotubes.[20,21] Among these nanostructures, gold nanorods (GNRs) have been extensively investigated as contrast and photothermal agents because of their superior optical properties, such as high absorption and tunable aspect-ratio dependent surface plasmon resonance (SPR) across the NIR region.[22,23] However, their biomedical applications are often limited, owing to the toxicity of the surfactant CTAB without further modification. Generally, in order to improve the biocompatibility of GNRs, an effective method is coating biocompatible shells on the surface of GNRs, such as silica or polymers.

Recently, polypyrrole (PPy), a new type of conductive and biocompatible material, has been widely used in biomedical applications.[24] Benefiting from its good biocompatibility and high conductivity, PPy as a shell material can increase the biosafety and stability of GNRs.[25] In addition, it has been

[a]*Key Laboratory of Design and Assembly of Functional Nanostructures, Fujian Institute of Research on the Structure of Matter, Chinese Academy of Sciences, Fuzhou 350002, China. E-mail: xiaoloong.liu@gmail.com; zhangy@fjirsm.ac.cn*

[b]*Department of Translational Medicine, Xiamen Institute of Rare Earth Materials, Chinese Academy of Sciences, Xiamen 361021, China*

[c]*The United Innovation of Mengchao Hepatobiliary Technology Key Laboratory of Fujian Province, Mengchao Hepatobiliary Hospital of Fujian Medical University, Fuzhou 350025, China*

† Electronic supplementary information (ESI) available. See DOI: 10.1039/c9ra00541b

‡ These authors contributed equally to this work.

reported that PPy is one of the best nanocarriers for drug delivery.[26,27] So, a combination of chemotherapy and photothermal therapy can be achieved in one nanoplatform by using PPy-coated GNRs. And the therapeutic effect can be further enhanced in comparison with PTT or chemotherapy alone.[28]

Besides, enrichment of nanomaterials at the tumor site can improve the killing effect on tumor cells. In order to enhance the tumor targeting and cellular uptake ability of our theranostic agent, folic acid (FA), a nonimmunogenic receptor-specific ligand, has emerged as an attractive specific ligand for targeted anticancer drug delivery, because folate receptors are often overexpressed on the surface of human cancer cells.[29,30] Furthermore, combining therapeutic and diagnostic modalities into a platform has evolved as a new paradigm in cancer therapies.[31] Thus, an ideal nanoplatform for cancer therapy should not only allow treatment by chemo-photothermal effect and targeted delivery of therapeutic agents, but also provide detailed information on tumor characteristics *via* various forms of bioimaging.[32,33] To this end, it is important to explore multifunctional therapeutic platforms by a combination of different imaging and therapy modalities for multimodal bioimaging-guided cancer therapies.

Therefore, in this study, we developed a multifunctional theranostic agent, GNR@PPy@Fe_3O_4-DOX-FA nanocomposites, which provided cell targeting through FA and magnetic field, for MRI/CT/PA triple mode imaging and chemo-photothermal therapy for hepatocellular carcinoma. GNRs were synthesized by the seed growth method, and were successfully encapsulated with PPy NPs *via* a facile aqueous dispersion polymerization using $FeCl_3$ as oxidant and polyvinylpyrrolidone (PVP) as a stabilizer. Then, Fe_3O_4 was produced by reaction of Fe^{3+} and Fe^{2+} with ammonium hydroxide on PPy *in situ*. The GNR@PPy@Fe_3O_4 nanocomposites were obtained and then modified with DOX and FA. GNRs can be used for CT and PA imaging and are also a good PTT agent; the Fe_3O_4 component can be used as an MRI contrast. DOX can be used for chemotherapy as an antineoplastic agent and Fe_3O_4 and folic acid can enhance the targeting of cancer cells. Our results showed that GNR@PPy@Fe_3O_4 nanocomposites had a high photothermal efficiency of 51.46%, and the cell viability of cancer cells decreased to 15.83% and 16.47% because of chemo-photothermal therapy by GNR@PPy@Fe_3O_4-DOX-FA nanocomposites. The combined functionalities have great potential in biomedical applications, showing a powerful way to personalize the treatment of diseases.

Materials and methods

Materials

Hexadecyltrimethylammonium bromide (CTAB, 99%), ascorbic acid (AA, 99.99% metal basis), silver nitrate ($AgNO_3$, >99%), sodium borohydride ($NaBH_4$, 99%), hydrogen tetrachloroaurate trihydrate ($HAuCl_4 \cdot 3H_2O$, 99.9% metal basis), doxorubicin (DOX) and polyvinylpyrrolidone (PVP, molecular weight: 40 000) were purchased from Sigma-Aldrich (St. Louis, MO, USA). (3-Aminopropyl) triethoxysilane (APTES, AR), ferric chloride hexahydrate ($FeCl_3 \cdot 6H_2O$, 99%), ammonium hydroxide ($NH_3 \cdot H_2O$, 25–28%) and pyrrole (Py) were obtained from Aladdin (Shanghai, China). Folic acid (FA, AR) was obtained from Xiya Reagent. Ultrapure water (18.2 MΩ resistivity) was obtained with a Milli-Q water purification system (Millipore, USA) and used throughout the experiments. Dulbecco's modified Eagle's medium (DMEM) and fetal bovine serum (FBS) were purchased from Thermo Scientific (Logan, Utah, USA). Penicillin and streptomycin, Cell Counting Kit-8 (CCK8), 4′,6-diamidino-2-phenylindole (DAPI) and trypsin were obtained from MesGenBiotech (Shanghai, China).

Characterization

Transmission electron microscopy (TEM) images were recorded on a JEM-2100 system. Fourier transform infrared spectra (FT-IR) were acquired on a Thermo Nicolet iS50 FT-IR Spectrometer. UV-Vis-NIR absorption spectra were obtained using an Agilent Cary 5000 UV-Vis-NIR Spectrophotometer. Inductively coupled plasma optical emission spectroscopy (ICP-OES) was used to measure the content of Au and Fe in the nanomaterials. The photothermal properties of GNR@PPy@Fe_3O_4 were acquired on an 808 nm laser (BWT: diode laser system) and the temperature was assessed by a thermocouple microprobe (STPC-510P, Xiamen Baidewo Technology Co., China). The MRI were recorded on a 9.4T (Bruker Biospec) Small Animal MR Imaging System. The PAI were acquired on Small Animal PA Imaging System (Endra's Nexus 128). The CT imaging was assessed by a Positron Emission Tomography/Computed Tomography Inveon PET/CT (Siemense) system.

Synthesis of gold nanorods (GNRs)

GNRs were synthesized by the seed growth method with little modification.[34] Briefly, the gold seeds were firstly synthesized by adding $HAuCl_4$ (10 mM, 0.25 mL) into the CTAB solution (39.8 mg mL^{-1}, 9.15 mL). Then, freshly prepared, ice-cold $NaBH_4$ (10 mM, 0.6 mL) was quickly injected into the $HAuCl_4$–CTAB solution under vigorous stirring for 2 min. Then, the seed solution was aged at room temperature for 1 h before use. To further grow GNRs, the CTAB solution was first prepared. 3.64 g of CTAB was dissolved in 100 mL of warm water at 60 °C. The solution was naturally cooled to 30 °C, and subsequently 5 mL of 10 mM $HAuCl_4$ solution was added. The mixture was kept undisturbed at 30 °C for 10 min, after which 1 mL of 10 mM $AgNO_3$ solution was added, and slowly stirred for 5 min. 2 mL of 0.5 M H_2SO_4 was then injected into the reaction system and stirred for 5 min. This was followed by the addition of 0.8 mL of 0.1 M ascorbic acid into the mixed solution, and the solution was vigorously stirred for 30 s until it became colourless. Finally, 0.24 mL of seed solution was injected into the growth solution. The resultant mixture was stirred for another 30 s and left undisturbed at 30 °C for 12 h for growth of GNRs. The reaction products were isolated by centrifugation at 8000 rpm for 30 min, and washed with ultrapure water twice. The precipitates were re-dispersed in 40 mL of ultrapure water. The GNRs prepared here had a longitudinal surface plasma resonance band centered at 798 nm modified with CTAB.

Preparation of GNR@PPy nanoparticles

4 mL of GNR solution was mixed with 36 mL of aqueous solution containing 200 mg of PVP and 80 mg of $FeCl_3$, by vigorous stirring and ultrasonication for 30 min. Then 20 μL of pyrrole was dropped into the solution and oxidative polymerization was carried out for 4 h at room temperature to obtain GNR@PPy nanoparticles. The solution was directly used in the next step to synthesize the GNR@PPy@Fe_3O_4 nanoparticles

Preparation of GNR@PPy@Fe_3O_4 nanocomposites

The temperature of the GNR@PPy nanoparticle solution was raised to 70 °C; then 1 mL of 1% $NH_3 \cdot H_2O$ was injected into the solution, under stirring by mechanical agitation. The resulting nanoparticles were washed three times with deionized water after magnetically-assisted precipitation to remove excess PPy and other reactants. The total weight of the composite was measured by weighing the completely dried form of the final GNR@PPy@Fe_3O_4 product.

DOX loading and modification with folic acid

4 mL of 1 mg mL^{-1} GNR@PPy@Fe_3O_4 nanocomposites was mixed with an equal volume of 1 mg mL^{-1} DOX solution by violently stirring for 24 h in the dark. The obtained GNR@PPy@Fe_3O_4-DOX nanocomposites were collected after centrifugation and washing with ethanol three times. The amount of DOX in the supernatant was measured by UV-Vis-NIR absorption spectra.

$$\text{DOX loading capacity (\%)} = \frac{\text{total DOX} - \text{free DOX content in supernatant}}{\text{weight of nanomaterials}} \times 100\% \quad (1)$$

0.2 mg mL^{-1} of FA and 20 μL of APTES were added into 6 mL of ethanol and stirred for 2 h in the dark. Then, 2 mL of GNR@PPy@Fe_3O_4-DOX solution was injected into the above solution under magnetic stirring for 12 h. In order to remove the excess reagents, the products of GNR@PPy@Fe_3O_4-DOX-FA nanocomposites were collected *via* centrifugation at 8500 rpm for 25 min and re-dispersed in 2 mL of ethanol.

DOX release

In order to explore the *in vitro* release kinetics of DOX, 2 mL aliquots of GNR@PPy@Fe_3O_4-DOX solution were respectively mixed with 20 mL of pH 4.8, 5.6, 6.6 and 7.4 PBS buffer solutions, and then the supernatants were collected by centrifugation after different periods of incubation time (0.5, 1, 1.5, 2, 4, 6, 12, 24 and 48 h). The release amount of DOX in the supernatant was measured by UV-Vis-NIR absorbance spectroscopy.

Photothermal test

To study the photothermal performance of GNR@PPy@Fe_3O_4 nanocomposites, 1 mL aliquots of aqueous solutions of the GNR@PPy@Fe_3O_4 nanocomposites at different concentrations (6.25, 12.5, 25, 50 and 100 μg mL^{-1}) were irradiated with an 808 nm laser at a power of 2 W for 10 min, where the spot area of the 808 nm laser was 1 cm^2. The temperatures of the solutions were monitored by a digital thermometer. Then, the photothermal conversion efficiency η was calculated with eqn (2), where T_{max} and T_{sur} are the maximum and initial temperatures of the solution, h is the heat-transfer coefficient, S is the area cross-section perpendicular to conduction, Q_{dis} is the outgoing thermal energy with laser power, I, and absorbance of GNR@PPy@Fe_3O_4 nanocomposites at a wavelength of 808 nm.[35]

$$\eta = \frac{hS(T_{max} - T_{sur}) - Q_{dis}}{I(1 - 10^{-A})} \quad (2)$$

Cytotoxicity and chemo-photothermal therapy evaluation

HepG2 and SMMC-7721 cells were cultured in Dulbecco's modified Eagle's medium (DMEM) with 10% fetal bovine serum (FBS), 100 mg mL^{-1} of penicillin and 100 mg mL^{-1} of streptomycin in a humidified atmosphere containing 5% CO_2 at 37 °C. The cytotoxicities of GNR@PPy@Fe_3O_4 and GNR@PPy@Fe_3O_4-FA nanocomposites against HepG2 and SMMC-7721 cells were determined with Cell Counting Kit-8 (CCK-8 kit). In a typical experiment, approximately 1×10^4 HepG2 or SMMC-7721 cells were seeded in 96-well culture plates and then incubated with different concentrations of GNR@PPy@Fe_3O_4 or GNR@PPy@Fe_3O_4-FA nanocomposites (50, 100, 150, 200, 250 and 300 μg mL^{-1}) for 24 h in a humidified chamber at 37 °C with 5% CO_2. Cell viabilities were evaluated with CCK-8 according to the manufacturer's protocol.

$$\text{Viability\%} = \frac{\text{mean absorbance value of treatment group}}{\text{mean absorbance value of control group}} \times 100\% \quad (3)$$

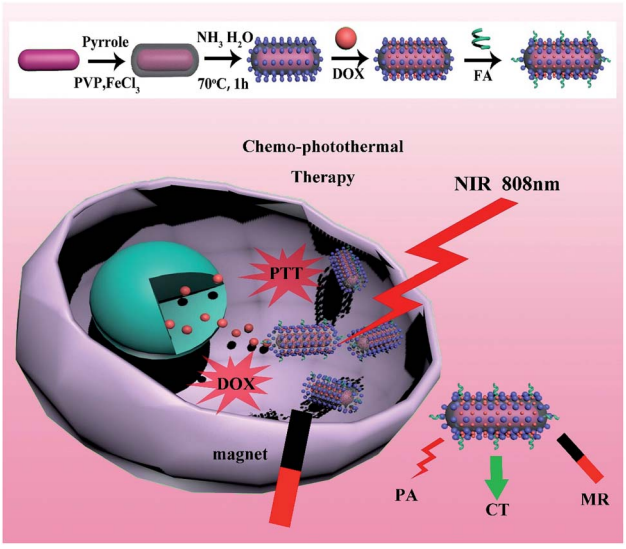

Fig. 1 Schematic illustration of synthetic route and chemo-photothermal therapy for GNR@PPy@Fe_3O_4-DOX-FA nanocomposites.

For photothermal therapy experiments, HepG2 or SMMC-7721 cells were incubated in 96-well plates at 37 °C in a humidified atmosphere containing 5% CO_2 for 24 h. The GNR@PPy@Fe_3O_4-FA and GNR@PPy@Fe_3O_4-DOX-FA nanocomposites at different concentrations (50, 100, 150, 200, 250 and 300 μg mL^{-1}) were added and the cells were further incubated for 24 h. With or without irradiation by an 808 nm laser (0.65 W) for 3 min, the cells were incubated at 37 °C for another 24 h. The cell viabilities were studied by standard CCK-8 assays.

In vitro cellular uptake

Briefly, 5×10^4 HepG2 cells were seeded into a cell culture dish and cultured for 24 h to allow the cells to attach. Afterwards, GNR@PPy@Fe_3O_4-DOX and GNR@PPy@Fe_3O_4-DOX-FA nanocomposites of a certain concentration were injected into fresh medium and incubated for some time with or without a magnet. Thereafter, cells were washed with PBS and fixed by 4% formaldehyde for 10 min. The cell nuclei were stained with DAPI (1 μg mL^{-1}). The fluorescence images of the cells were acquired using a confocal laser scanning microscope (CLSM). And inductively coupled plasma optical emission spectroscopy (ICP-OES) was used to measure the concentration of Au and Fe after cellular uptake.

In vitro MR, CT and PA imaging

In vitro CT imaging of GNR@PPy@Fe_3O_4-FA nanocomposites was carried out by a Positron Emission Tomography/Computed Tomography (Siemens Inveon PET/CT) system. The samples were diluted in water and the concentrations of Au (determined by ICP-MS) were 0.21, 0.42, 0.84, 1.68, 3.36 and 6.72 mM. The control sample was fixed with 1% agar and water. The CT images and obtained CT values were analysed.

In vitro MR imaging of GNR@PPy@Fe_3O_4-FA nanocomposites was studied in a Bruker 9.4T Biospec Small Animal MR Imaging System. Using water as the reference, the concentrations of Fe (determined by ICP-MS) in the samples were 0.03, 0.06, 0.12, 0.25, 0.49, 0.98 and 1.97 mM, respectively. The T_2 relaxivity value (r_2) of GNR@PPy@Fe_3O_4-FA was calculated by linear fitting of $1/T_2$ and the concentration of Fe.

In order to study the *in vitro* PA imaging function of the GNR@PPy@Fe_3O_4-FA nanocomposites, *in vitro* PA imaging experiments were carried out on an Endra Nexus 128 Fully 3-D Photoacoustic CT Scanner. The PAI data of aqueous solutions containing different concentrations (0.016, 0.032, 0.063, 0.125 and 0.25 mg mL^{-1}) of GNR@PPy@Fe_3O_4-FA nanocomposites were obtained under 808 nm laser irradiation. The data were analysed with the corresponding software, and the PA images and PA signal values of the GNR@PPy@Fe_3O_4-FA nanocomposites were acquired.

In vivo multimodal imaging

Female mice were purchased from China Wushi, Inc. (Shanghai, China). All animal procedures were performed in accordance with the Guidelines for Care and Use of Laboratory Animals of Xiamen University and approved by the Animal Ethics Committee of Xiamen University. 100 μL of ascites was injected into each mouse. When the tumour volume was about 100 mm^3, GNR@PPy@Fe_3O_4-FA (2 mg mL^{-1}, 100 μL) was injected through the tail vein. CT/MR/PA multimodal imaging was carried out before and 24 h after injection.

In vivo chemo-photothermal therapy evaluation

To further prove the potential of the GNR@PPy@Fe_3O_4-DOX-FA nanocomposites for *in vivo* cancer therapy, the tumor-bearing mice were divided into six groups (three mice per group): (1) control group (intravenous injection with PBS), (2) intravenous injection with GNR@PPy@Fe_3O_4 (100 μL, 2 mg mL^{-1}), (3) GNR@PPy@Fe_3O_4-DOX-FA (100 μL, 2 mg mL^{-1}), (4) GNR@PPy@Fe_3O_4-DOX (100 μL, 2 mg mL^{-1}) + laser, (5) GNR@PPy@Fe_3O_4-FA (100 μL, 2 mg mL^{-1}) + laser, (6) GNR@PPy@Fe_3O_4-DOX-FA (100 μL, 2 mg mL^{-1}) + laser. The laser irradiation was applied to the tumor area (2 W cm^{-2}, 5

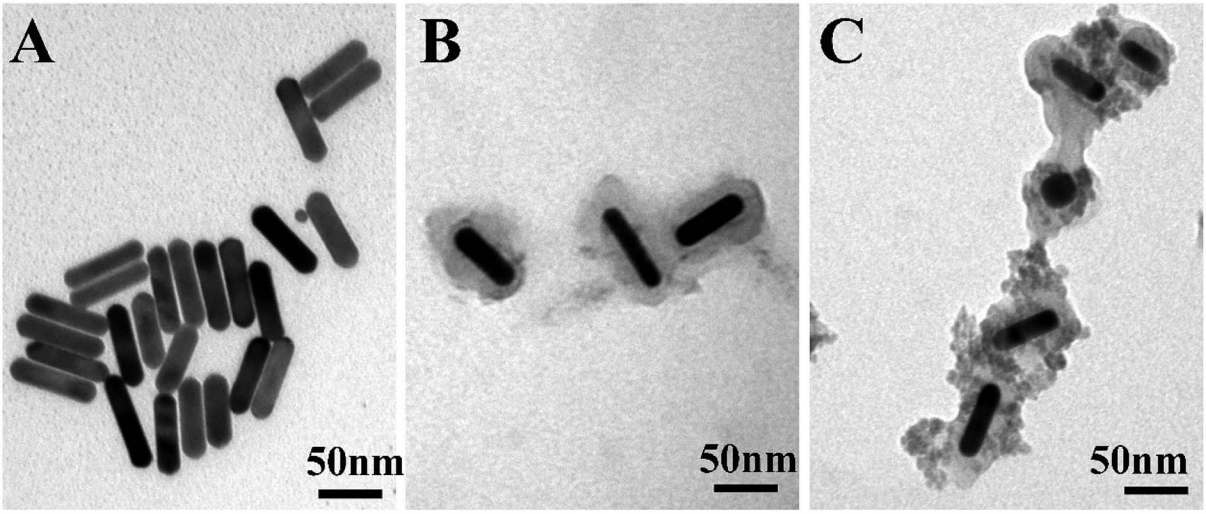

Fig. 2 TEM images of (A) GNRs, (B) GNR@PPy nanoparticles, and (C) GNR@PPy@Fe_3O_4 nanocomposites.

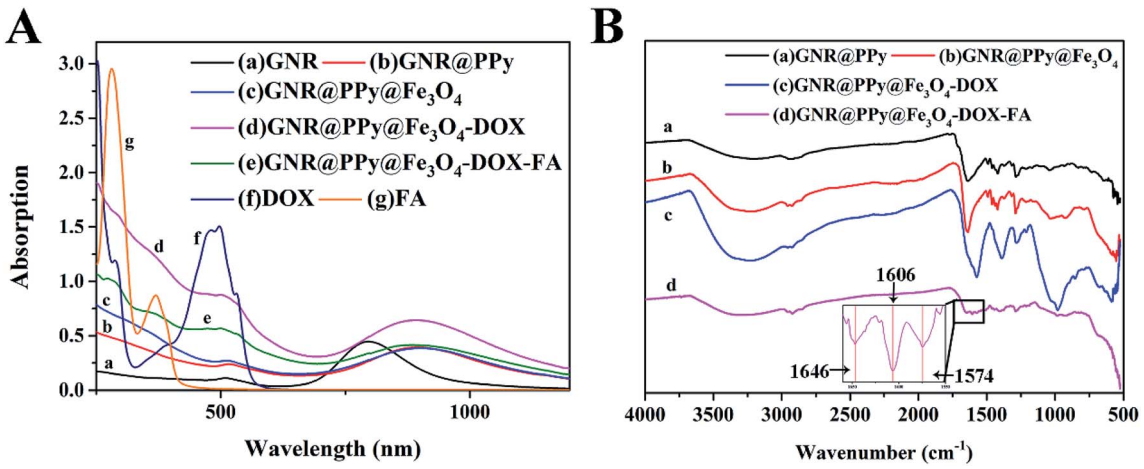

Fig. 3 (A) UV-Vis-NIR absorption spectra of GNRs (a), GNR@PPy (b), GNR@PPy@Fe_3O_4 (c), GNR@PPy@Fe_3O_4-DOX (d), GNR@PPy@Fe_3O_4-DOX-FA (e), DOX (f) and FA (g) nanocomposites, where the concentrations of these nanocomposites were about 40 μg mL^{-1}; (B) the FTIR spectra of the prepared GNR@PPy (a), GNR@PPy@Fe_3O_4 (b), GNR@PPy@Fe_3O_4-DOX (c) and GNR@PPy@Fe_3O_4-DOX-FA (d) nanocomposites. The inset shows the characteristic peaks of GNR@PPy@Fe_3O_4-DOX-FA nanocomposites at 1646 cm^{-1}, 1606 cm^{-1} and 1574 cm^{-1}. Inset is the spectrum in the wavenumber range of 1550–1660 cm^{-1}.

min) 24 h after intravenous injection. The changes in tumor volume and body weight were measured every two days.

Results and discussion

Synthesis of GNR@PPy@Fe_3O_4 nanocomposites

The overall procedure for the formation of GNR@PPy@Fe_3O_4 nanocomposites is illustrated in Fig. 1. The CTAB-capped GNRs were firstly synthesized by the seed growth method, and then GNRs were introduced to a solution of PVP and $FeCl_3$. Next, the pyrrole monomers were added into the complex solution. The PPy shell was coated onto the surface of the GNRs *via* oxidative polymerization using $FeCl_3$ as an oxidation agent and PVP as a capping agent and dispersion aid.[36] Furthermore, we utilized unreacted Fe^{3+} and reduced Fe^{2+} ions to produce Fe_3O_4 crystals *in situ* on the surface of GNR@PPy nanoparticles without any additional iron precursors by using the coprecipitation method.

Characterizations of GNR@PPy@Fe_3O_4-DOX-FA nanocomposites

TEM was used to study the structure of the GNR@PPy@Fe_3O_4 nanocomposites. As shown in Fig. 2A, the GNRs were about 57.98 nm in length and about 13.9 nm in width, and the average aspect ratio (length to diameter ratio) of the GNRs was 4.0. After the reaction, GNRs were coated with PPy, and the thickness of the PPy layer was about 16.17 nm (Fig. 2B). As shown in Fig. 2C, GNR@PPy@Fe_3O_4 nanocomposites with a well-defined structure were successfully synthesized. ICP-OES was used to analyse the elements in the GNR@PPy@Fe_3O_4 nanocomposites. The amounts of Au and Fe in the GNR@PPy@Fe_3O_4 nanocomposites were about 23.59% and 31.52%, respectively. The particle size distributions of GNR@PPy@Fe_3O_4-DOX-FA in water and PBS were also found. As shown in Fig. S1,† the effective diameters of GNR@PPy@Fe_3O_4-DOX-FA in water and PBS were 118 nm and 137 nm, respectively. The results indicated that the GNR@PPy@Fe_3O_4-DOX-FA nanocomposites have good dispersion in water and phosphate buffer saline (PBS) solutions.

Fig. 3A shows the UV-Vis-NIR absorption spectra of GNRs, and GNR@PPy, GNR@PPy@Fe_3O_4, GNR@PPy@Fe_3O_4-DOX and GNR@PPy@Fe_3O_4-DOX-FA nanocomposites. The GNRs had two absorbance peaks at 509 and 798 nm, which match the TEM images in Fig. 2A. After coating with PPy, a clear red shift in the absorption spectra of GNR@PPy and GNR@PPy@Fe_3O_4 nanocomposites was observed. The reason is that the PPy shell alters the localized electric field distribution of the GNRs. GNR@PPy@Fe_3O_4-DOX and GNR@PPy@Fe_3O_4-DOX-FA still exhibited strong NIR absorbance, and the GNRs showed a characteristic absorption peak of DOX near 480 nm, indicating that the DOX was successfully loaded onto

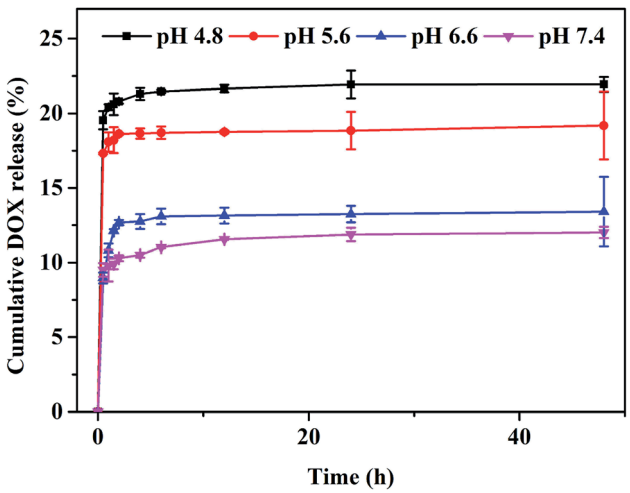

Fig. 4 DOX release profile of GNR@PPy@Fe_3O_4-DOX nanocomposites at different pH values.

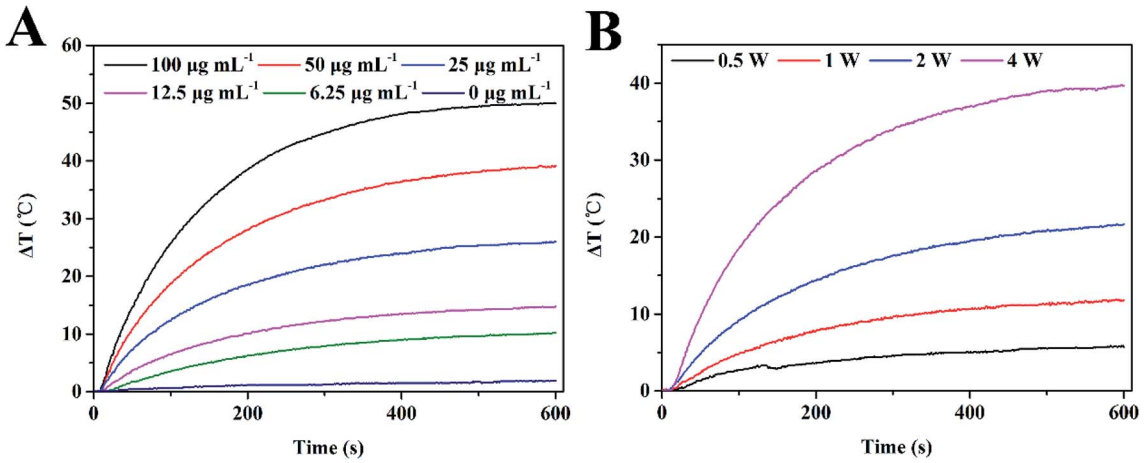

Fig. 5 Photothermal effect of GNR@PPy@Fe_3O_4 nanocomposites. (A) Photothermal heating curves of GNR@PPy@Fe_3O_4 nanocomposites with different concentrations exposed to 808 nm laser irradiation for 10 min at a power of 2 W; (B) photothermal characteristics of 25 μg mL^{-1} GNR@PPy@Fe_3O_4 nanocomposites under 808 nm laser irradiation at various powers for 10 min.

GNR@PPy@Fe_3O_4. Moreover, FA had a typical absorption peak at 280 nm, which was observed in the GNR@PPy@Fe_3O_4-DOX-FA nanocomposites, demonstrating that FA was successfully conjugated onto GNR@PPy@Fe_3O_4-DOX.

In addition, the characteristic bond vibrations of the samples were identified by using FTIR spectroscopy (Fig. 3B). For GNR@PPy nanocomposites, the characteristic peaks of 1287 and 1421 cm^{-1} corresponded to the C–H stretching

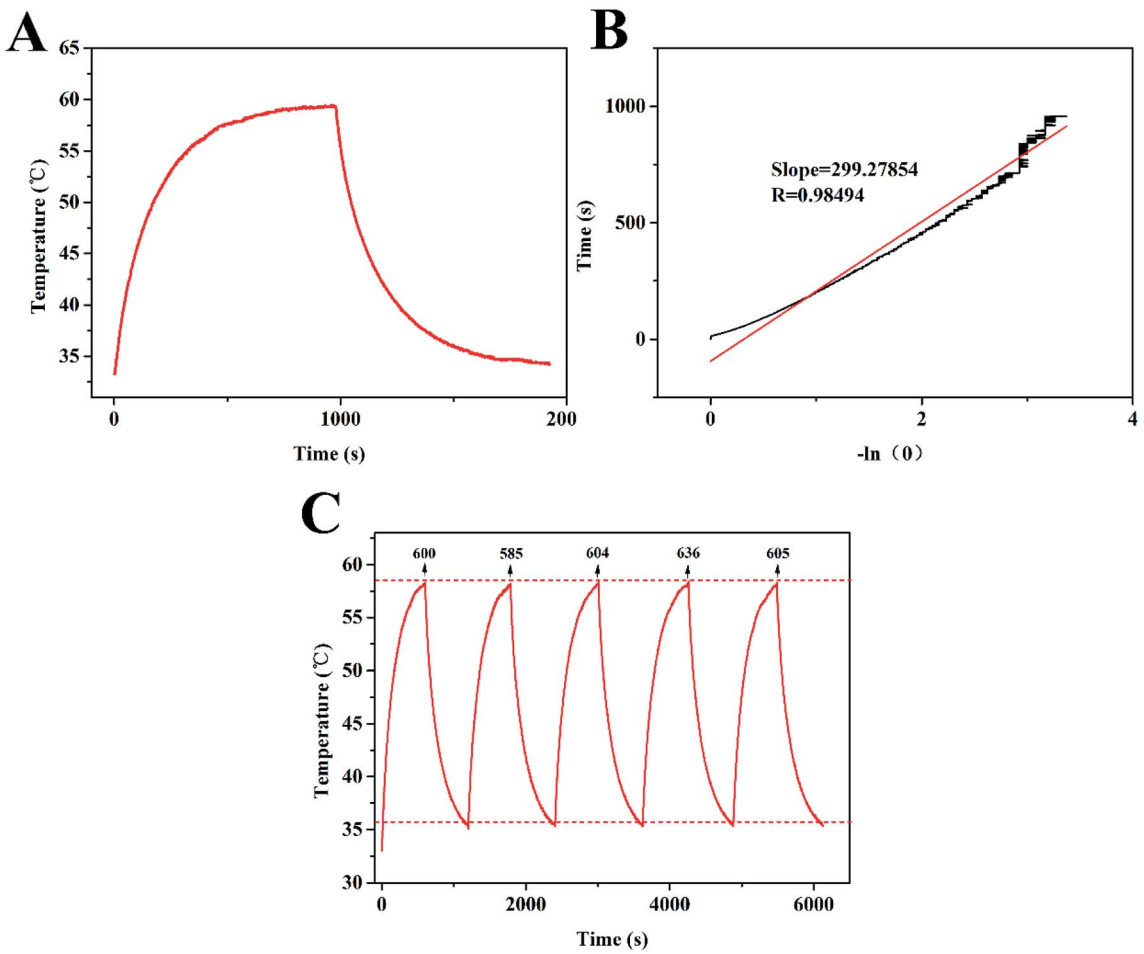

Fig. 6 (A) The temperature change curve of GNR@PPy@Fe_3O_4 aqueous solutions under 808 nm laser irradiation for 10 min; (B) the corresponding linear fitting of the irradiation time obtained from the cooling phase and $-\ln(\theta)$; (C) evaluation of photothermal stability of GNR@PPy@Fe_3O_4 nanocomposites at a concentration of 25 μg mL^{-1} through five cycles of an on-and-off laser.

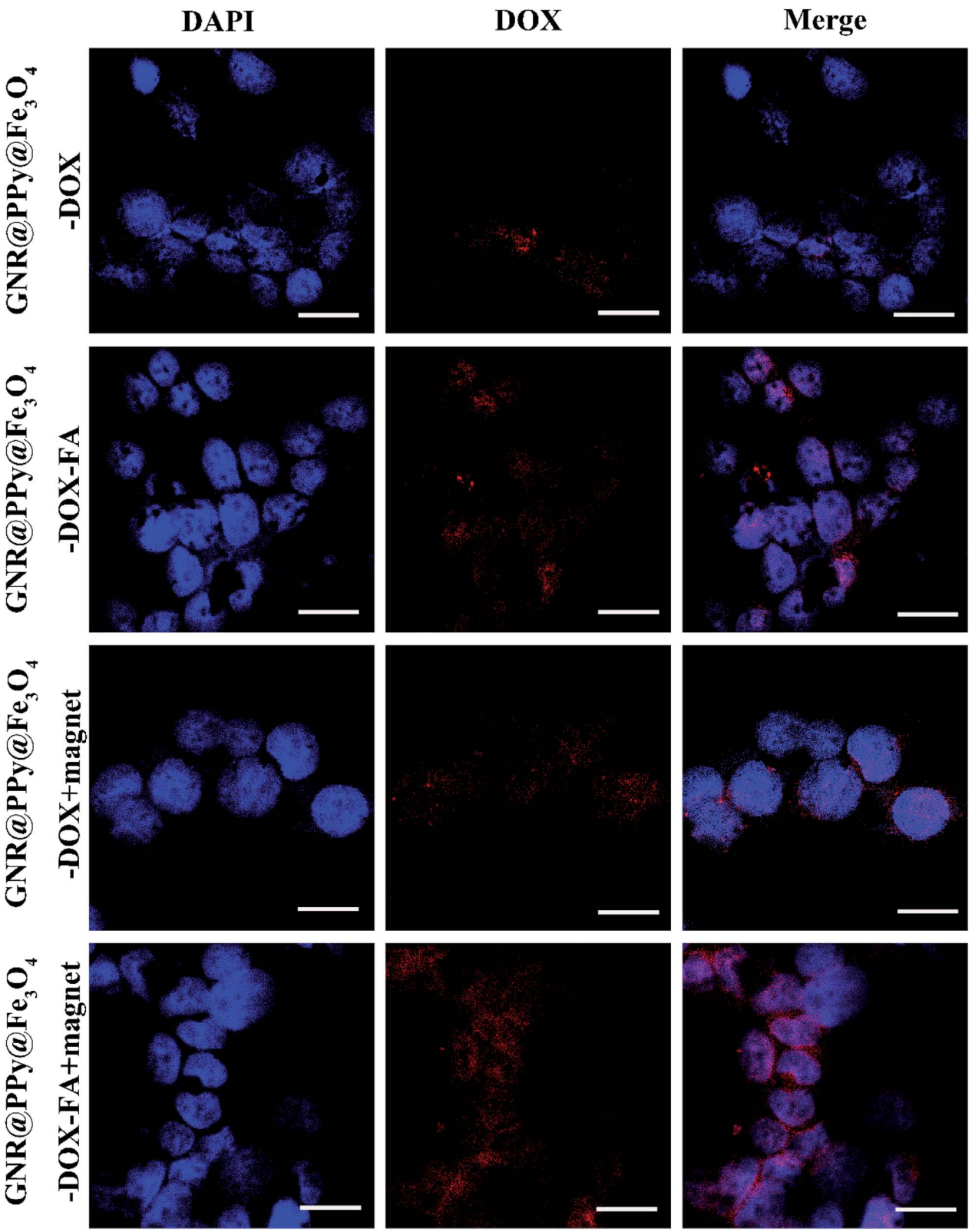

Fig. 7 CLSM images of HepG2 cells incubated with 200 μg mL^{-1} GNR@PPy@Fe_3O_4-DOX and GNR@PPy@Fe_3O_4-DOX-FA nanocomposites for 4 h with or without an external magnetic field. Scale bar: 20 μm.

vibration and N–H deformation vibration of polypyrrole, respectively. The peak at 1640 cm^{-1} was related to the stretching vibration of C=O, which was affected by the surfactant PVP. Compared with the GNR@PPy nanocomposites, the FTIR spectra of the GNR@PPy@Fe_3O_4 nanocomposites showed a characteristic absorption peak of Fe–O at 553 cm^{-1},

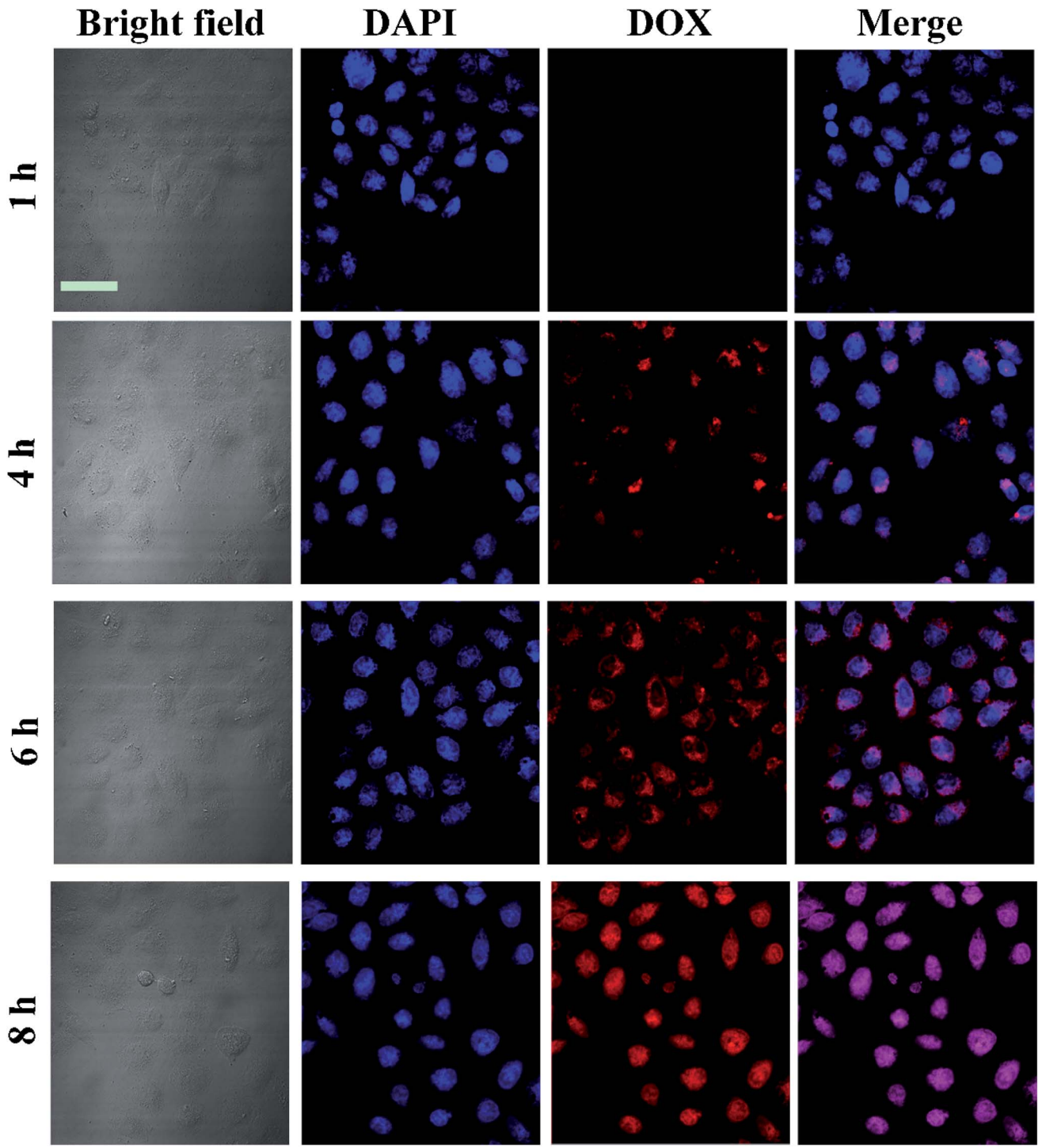

Fig. 8 CLSM images of HepG2 cells incubated with 300 μg mL^{-1} GNR@PPy@Fe_3O_4-DOX-FA nanocomposites for 1, 4, 6 and 8 h. Scale bar: 50 μm.

confirming that we had successfully synthesized GNR@PPy@Fe_3O_4 nanocomposites. The characteristic peaks of 1210 cm^{-1} and 981 cm^{-1} were attributed to the bending vibrations of C–H and C–C=O of DOX, which verified the successful loading of DOX onto the GNR@PPy@Fe_3O_4 nanocomposites.[37] In addition, the FTIR spectrum of GNR@PPy@Fe_3O_4-DOX-FA displayed the C=O stretching vibration and benzene skeleton vibration at 1646 cm^{-1} and 1606 cm^{-1}, confirming the successful conjunction of FA on the surface of the GNR@PPy@Fe_3O_4 nanocomposites.[38]

DOX loading and release

To further investigate the drug loading and release of GNR@PPy@Fe_3O_4 nanocomposites, DOX was loaded onto the surface of GNR@PPy@Fe_3O_4 nanocomposites by simply mixing

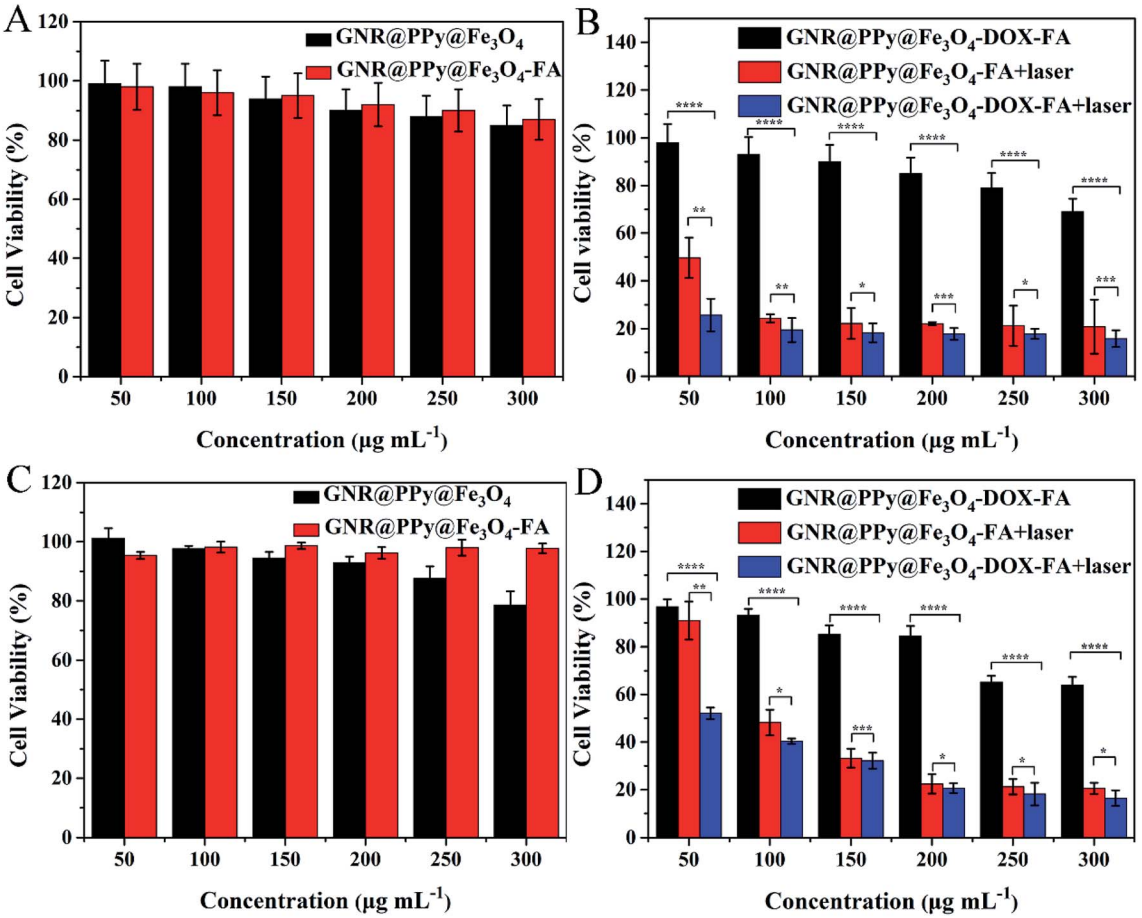

Fig. 9 Cell viabilities of HepG2 (A) and SMMC-7721 (C) cells treated with different concentrations of GNR@PPy@Fe_3O_4 and GNR@PPy@Fe_3O_4-FA nanocomposites. Viabilities of HepG2 (B) and SMMC-7721 (D) cells after incubation with different concentrations of GNR@PPy@Fe_3O_4-FA and GNR@PPy@Fe_3O_4-DOX-FA nanocomposites with or without 808 nm laser irradiation. The p values were calculated using multiple t tests (*p < 0.05, **p < 0.01, ***p < 0.001, ****p < 0.0001).

DOX aqueous solutions overnight to form GNR@PPy@Fe_3O_4-DOX nanocomposites. The DOX concentration was determined from the typical absorption peak of DOX at about 480 nm with the established standard curve (Fig. S2†). The loading capacity of DOX was 11.37%. To test the DOX release profile, GNR@PPy@Fe_3O_4-DOX was dispersed in PBS at all pH values of 4.8, 5.6, 6.6 and 7.4.[39] As shown in Fig. 4, the release amount of DOX at pH 7.4 was only about 12.01% over 48 h. However, about 23.64%, 19.19% and 13.41% DOX were released at pH 4.8, 5.6 and 6.6 over 48 h. The pH-dependent drug release of DOX from GNR@PPy@Fe_3O_4-DOX nanocomposites is beneficial for cancer therapy.

Photothermal properties of GNR@PPy@Fe_3O_4 nanocomposites

The strong absorption of GNR@PPy@Fe_3O_4 nanocomposites in the NIR area motivated us to explore their NIR photothermal properties. The photothermal effect of GNR@PPy@Fe_3O_4 nanocomposites was investigated by measuring the temperature changes in GNR@PPy@Fe_3O_4 solution at various concentrations (0, 6.25, 12.5, 25, 50 and 100 μg mL^{-1}) under 808 nm laser irradiation (2 W). As shown in Fig. 5A, with an increase in the concentration of GNR@PPy@Fe_3O_4 nanocomposites or NIR laser irradiation time, the temperature of the solutions increased rapidly. Furthermore, the temperature of the GNR@PPy@Fe_3O_4 solution (25 μg mL^{-1}) showed a 25.7 °C increase (from 32.6 °C to 58.3 °C) after 808 nm laser irradiation for 10 min, while the pure water showed negligible changes. Moreover, GNR@PPy@Fe_3O_4 nanocomposites displayed an obvious laser-power-dependent photothermal effect (Fig. 5B). These data indicated that GNR@PPy@Fe_3O_4 could act as an efficient photothermal coupling agent. Subsequently, in order to further study, the photothermal conversion properties of GNR@PPy@Fe_3O_4, 25 μg mL^{-1} of GNR@PPy@Fe_3O_4 aqueous solution was continuously exposed to near infrared light and then naturally cooled to room temperature after rising to its highest temperature (Fig. 6A and B). According to the obtained data, the photothermal conversion efficiency of the GNR@PPy@Fe_3O_4 nanocomposites was calculated to be about 51.46%. As shown in Fig. 6C, the photothermal conversion efficiency of the GNR@PPy@Fe_3O_4 nanocomposites remained stable without significant changes after five laser irradiation

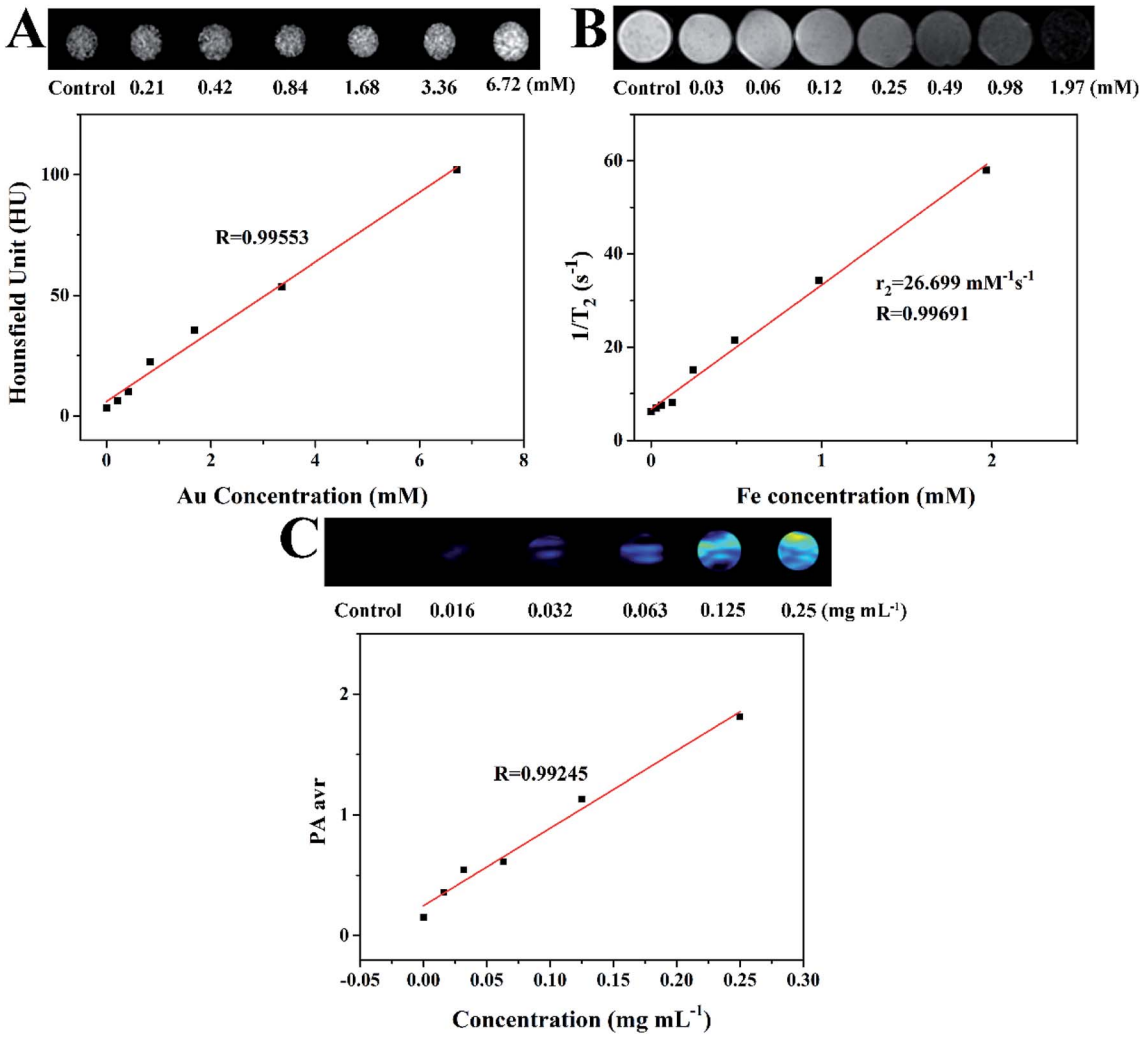

Fig. 10 (A) CT images of GNR@PPy@Fe_3O_4-FA nanocomposites with different Au concentrations and their CT values (HU) as a function of Au concentration. (B) T_2-weighted MRI photographs of GNR@PPy@Fe_3O_4-FA nanocomposites dispersed in water with different Fe concentrations and the transverse relaxation rate ($1/T_2$) as a function of Fe concentration (C) PA images and corresponding PA intensity of GNR@PPy@Fe_3O_4-FA nanocomposites of different concentrations. The PA signal values at different concentrations were obtained by using an 808 nm laser.

cycles, indicating that GNR@PPy@Fe_3O_4 had good photostability.

In vitro cellular uptake of GNR@PPy@Fe_3O_4-DOX-FA nanocomposites

Prior to investigation of the as synthesized nanocomposites for further therapy applications, the GNR@PPy@Fe_3O_4-DOX-FA nanocomposites were incubated with HepG2 to evaluate their cell uptake behaviour. After incubation for 4 h, the cells were collected and the cellular red fluorescence of DOX was visualized by a confocal laser scanning microscope (CLSM). Fig. 7 shows that the fluorescence intensity of HepG2 cells treated with GNR@PPy@Fe_3O_4-DOX-FA was considerably higher than that of GNR@PPy@Fe_3O_4-DOX, indicating that folic acid enhanced the targeting of the composite nanomaterials to the cells. Moreover, the cellular uptake of GNR@PPy@Fe_3O_4-DOX-FA under the influence of an external magnetic field was higher than that without the magnetic field. The cellular uptakes of Au and Fe are listed in Table S1.† The amounts of Au and Fe increased with a magnetic field. In addition, the cellular uptake of GNR@PPy@Fe_3O_4-DOX-FA exhibited time-dependent behavior (Fig. 8). These results suggested that the GNR@PPy@Fe_3O_4-DOX-FA nanocomposites can be efficiently taken up by cancer cells and enable specifically targeted delivery of DOX into cancer cells *via* FA and magnetically targeted.

Cytotoxicity evaluation and chemo-photothermal therapy

In order to achieve further bioapplications of the GNR@PPy@Fe_3O_4-FA nanocomposites, their biocompatibility was a primary concern. Therefore, the cell viability for HepG2 and SMMC-7721 cells incubated with GNR@PPy@Fe_3O_4 or GNR@PPy@Fe_3O_4-FA nanocomposites at different concentrations for 24 h was determined by CCK-8 assay. Fig. 9A and C show the high cell viabilities of HepG2 and SMMC-7721 cells even when the concentrations of GNR@PPy@Fe_3O_4 or GNR@PPy@Fe_3O_4-FA nanocomposites reached 300 μg mL^{-1}.

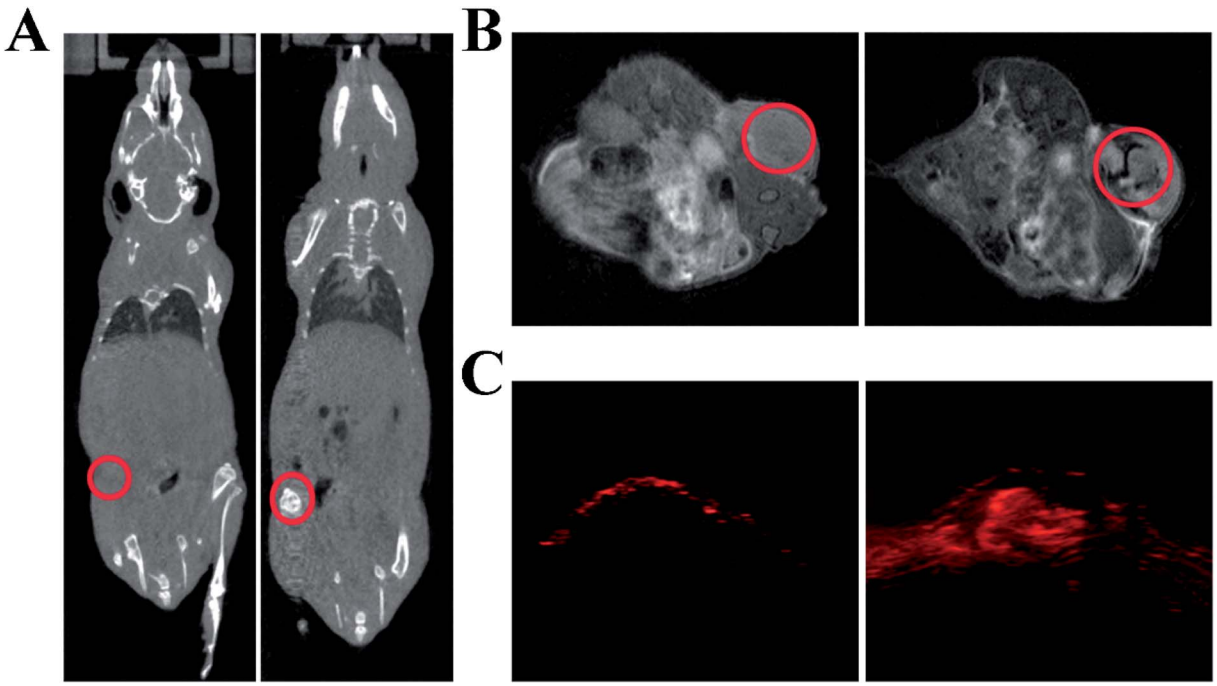

Fig. 11 *In vivo* CT images (A), MR images (B) and PA images (C) of GNR@PPy@Fe_3O_4-FA nanocomposites before and 24 h after injection.

This meant that GNR@PPy@Fe_3O_4 and GNR@PPy@Fe_3O_4-FA had low toxicity against HepG2 and SMMC-7721 cells, confirming that GNR@PPy@Fe_3O_4 and GNR@PPy@Fe_3O_4-FA nanocomposites had good biocompatibility.

Furthermore, to evaluate the effect of chemo-photothermal therapy *in vitro*, HepG2 or SMMC-7721 cells were incubated with different concentrations of GNR@PPy@Fe_3O_4-FA and GNR@PPy@Fe_3O_4-DOX-FA for 24 h. Then the cells were treated with or without NIR irradiation. Subsequently, the cells were incubated for another 24 h and a CCK-8 assay was carried out to test cell viability. As shown in Fig. 9B and D, after 808 nm laser irradiation (0.65 W), the GNR@PPy@Fe_3O_4-DOX-FA nanocomposites exhibited a higher cell killing effect in HepG2 and SMMC-7721 cells at all tested concentrations than the GNR@PPy@Fe_3O_4-DOX-FA without laser irradiation or the GNR@PPy@Fe_3O_4-FA with laser irradiation. The results indicated that the therapeutic effect of chemo-photothermal therapy was better than that of chemotherapy or photothermal therapy alone, demonstrating the synergistic effect of chemo-photothermal treatment.

In vitro multimode imaging of GNR@PPy@Fe_3O_4-FA nanocomposites

Because gold nanomaterials can be employed as CT imaging contrast agents, we measured the CT contrast efficacy of as-synthesized GNR@PPy@Fe_3O_4-FA nanocomposites. As shown in Fig. 10A, the enhancement effect of GNR@PPy@Fe_3O_4-FA with different concentrations of Au on CT imaging was studied. The signal intensity of GNR@PPy@Fe_3O_4-FA increased with an increase in Au concentration. The CT values of GNR@PPy@Fe_3O_4-FA were linearly related to the concentration of Au in the materials, which indicated that GNR@PPy@Fe_3O_4-FA nanocomposites can be used as a contrast agent for CT imaging.

The potential of GNR@PPy@Fe_3O_4-FA nanocomposites as multimode imaging contrast agents was further researched. The *in vitro* MR imaging ability of GNR@PPy@Fe_3O_4-FA nanocomposites was investigated by a Bruker 9.4T Biospec Small Animal MR Imaging System. As shown in Fig. 10B, the images revealed a clear iron-concentration-dependent darkening effect (the concentration of Fe was measured by ICP-OES). With the increase in Fe concentration, the T_2 signal intensity was significantly decreased. In addition, the transverse relaxation rate ($r_2 = 1/T_2$) was linearly related to Fe concentration. The transverse relaxation rate of the GNR@PPy@Fe_3O_4-FA nanocomposites was calculated to be 26.7 mM^{-1} s^{-1}. These results demonstrated that GNR@PPy@Fe_3O_4-FA nanocomposites showed promise for use as a T_2-weighted negative contrast agent for MRI.

The strong NIR absorption of GNRs and PPy motivated us to study the PA property of the GNR@PPy@Fe_3O_4-FA nanocomposites. Fig. 10C shows that the PA signal increased gradually with an increasing concentration of GNR@PPy@Fe_3O_4-FA at 808 nm, suggesting that the GNR@PPy@Fe_3O_4-FA nanocomposites would be good as a contrast agent for PAI applications.

In vivo multimodal imaging and chemo-photothermal therapy of GNR@PPy@Fe_3O_4-FA nanocomposites

As a proof-of-concept experiment, we next utilized GNR@PPy@Fe_3O_4-FA nanocomposites as a contrast agent for *in*

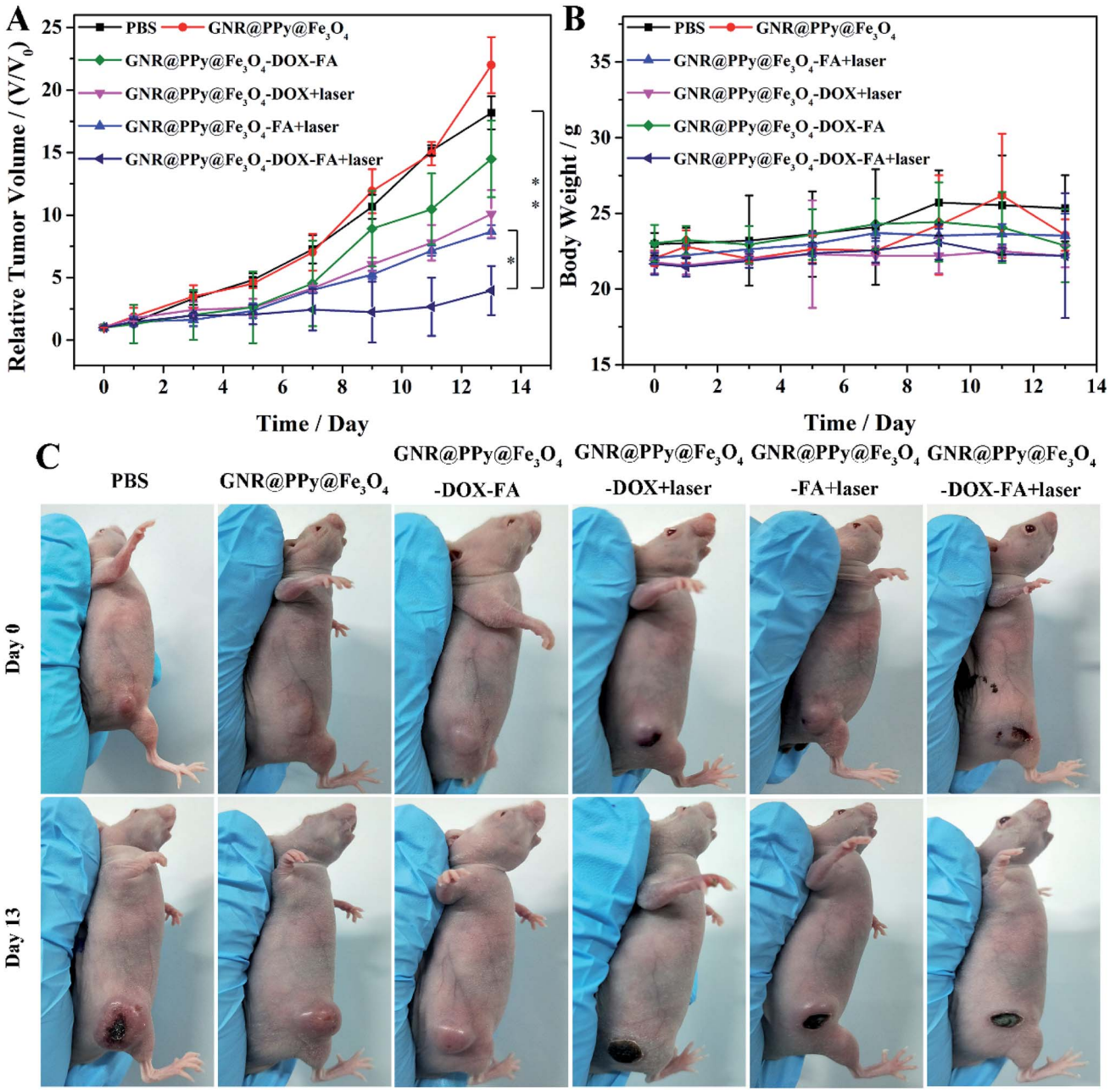

Fig. 12 (A) Tumor growth curves of different groups after various treatments. The p values were calculated using multiple t tests (*$p < 0.05$, **$p < 0.01$). (B) Body weights of mice in different treatment groups; (C) representative photographs of different groups of mice on days 0 and 13 after various treatments.

vivo CT/MR/PA multimodal imaging. The CT, MR and PA images were performed before and after intravenous injection with GNR@PPy@Fe_3O_4-FA nanocomposites into tumor-bearing mice. As shown in Fig. 11A, the CT signal in tumor tissue was greatly enhanced 24 h after injection with GNR@PPy@Fe_3O_4-FA. Then, the *in vivo* MRI contrast effects of GNR@PPy@Fe_3O_4-FA were investigated on a 9.4T MRI instrument. An obvious darkening effect at the tumor site was observed after the administration of GNR@PPy@Fe_3O_4-FA nanocomposites. Consistent with the CT and MRI findings, the PA signal in the tumor region was also significantly enhanced after intravenous injection with the nanocomposites. These results demonstrated that GNR@PPy@Fe_3O_4-FA nanocomposites could be a promising multimodal contrast agent for *in vivo* CT, MR and PA bioimaging.

Then, we examined the effect of chemo-photothermal therapy *in vivo*. It can be seen in Fig. 12 that the tumor growth was significantly inhibited in mice intravenously injected with GNR@PPy@Fe_3O_4-DOX-FA after NIR laser irradiation. However, tumors in other treatment groups showed relatively rapid growth. These results demonstrated that GNR@PPy@Fe_3O_4-DOX-FA could be a promising agent for combined PTT and chemotherapy *in vivo*.

Conclusions

In summary, we have successfully synthesized GNR@PPy@Fe_3O_4-DOX-FA nanocomposites as multifunctional theranostic agents for targeted multimodal imaging and chemo-photothermal therapy. The obtained nanocomposites have good water dispersion, high photothermal conversion efficiency and low cytotoxicity. Furthermore, GNR@PPy@Fe_3O_4-FA nanocomposites have the potential to be used as contrast agents for CT, MR and PA imaging. In combination with photothermal therapy and chemotherapy, GNR@PPy@Fe_3O_4-DOX-FA nanocomposites can effectively kill tumor cells and achieve excellent tumor therapy. The targeting ability of GNR@PPy@Fe_3O_4-DOX-FA nanocomposites can also reduce the damage to normal tissue during tumor therapy. Therefore, the synthesized GNR@PPy@Fe_3O_4-DOX-FA nanocomposites with multimodal imaging and chemo-photothermal therapy properties shows great potential in the integration of tumor diagnosis and treatment.

Conflicts of interest

The authors declare no competing financial interest.

Acknowledgements

The work was supported by the National Natural Science Foundation of China (No. 61605209), the Science and Technology Service Network Initiative Foundation of CAS (No. 2016T3009), the Pilot Project of Fujian Province of China (No. 2017Y0084), the Selfcreated Area Project of Major Science Technology Innovation Platform of Xiamen (No. 3502ZCQ20171002) and the Project of Collaborative Innovation of Industry-University-Research Institute and Science and Technology Cooperation of Xiamen (No.3502Z20182021).

References

1 S. D. Jo, S. H. Ku, Y. Y. Won, S. H. Kim and I. C. Kwon, *Theranostics*, 2016, **6**, 1362–1377.
2 N. Muhamad, T. Plengsuriyakarn and K. Na-Bangchang, *Int. J. Nanomed.*, 2018, **13**, 3921–3935.
3 V. Shanmugam, S. Selvakumar and C. S. Yeh, *Chem. Soc. Rev.*, 2015, **45**, 6254–6287.
4 L. Cheng, C. Wang, Z. Liu and S. University, *Chin. J. Clin. Oncol.*, 2014, **114**, 10869–10939.
5 J. Tang, R. Zhang, M. Guo, L. Shao, Y. Liu, Y. Zhao, S. Zhang, Y. Wu and C. Chen, *Biomaterials*, 2018, **167**, 205–215.
6 X. Cheng, R. Sun, L. Yin, Z. Chai, H. Shi and M. Gao, *Adv. Mater.*, 2017, **29**, 1604894.
7 J. Chen, X. Li, X. Zhao, Q. Q. Wu, H. Zhu, Z. Mao and C. Gao, *Bioact. Mater.*, 2018, **3**, 347–354.
8 X. Wang, H. Li, X. Liu, Y. Tian, H. Guo, T. Jiang, Z. Luo, K. Jin, X. Kuai, Y. Liu, Z. Pang, W. Yang and S. Shen, *Biomaterials*, 2017, **143**, 130–141.
9 Z. Bao, X. Liu, Y. Liu, H. Liu and K. Zhao, *Asian J. Pharm. Sci.*, 2016, **11**, 349–364.
10 W. I. Choi, J. Y. Kim, C. Kang, C. C. Byeon, Y. H. Kim and G. Tae, *ACS Nano*, 2011, **5**, 1995–2003.
11 S. Y. Liu, Z. S. Liang, F. Gao, S. F. Luo and G. Q. Lu, *J. Mater. Sci.: Mater. Med.*, 2010, **21**, 665–674.
12 M. F. Tsai, S. H. Chang, F. Y. Cheng, V. Shanmugam, Y. S. Cheng, C. H. Su and C. S. Yeh, *ACS Nano*, 2013, **7**, 5330–5342.
13 Y. Su, X. Wei, F. Peng, Y. Zhong, Y. Lu, S. Su, T. Xu, S. T. Lee and Y. He, *Nano Lett.*, 2012, **12**, 1845–1850.
14 K. Yang, S. Zhang, G. Zhang, X. Sun, S. T. Lee and Z. Liu, *Nano Lett.*, 2010, **10**, 3318–3323.
15 D. K. Lim, A. Barhoumi, R. G. Wylie, G. Reznor, R. S. Langer and D. S. Kohane, *Nano Lett.*, 2013, **13**, 4075–4079.
16 J. T. Robinson, S. M. Tabakman, Y. Liang, H. Wang, H. S. Casalongue, D. Vinh and H. Dai, *J. Am. Chem. Soc.*, 2011, **133**, 6825–6831.
17 M. Zhou, R. Zhang, M. Huang, W. Lu, S. Song, M. P. Melancon, M. Tian, D. Liang and C. Li, *J. Am. Chem. Soc.*, 2010, **132**, 15351–15358.
18 Q. Tian, M. Tang, Y. Sun, R. Zou, Z. Chen, M. Zhu, S. Yang, J. Wang, J. Wang and J. Hu, *Adv. Mater.*, 2011, **23**, 3542–3547.
19 C. M. Hessel, V. P. Pattani, M. Rasch, M. G. Panthani, B. Koo, J. W. Tunnell and B. A. Korgel, *Nano Lett.*, 2011, **11**, 2560–2566.
20 J. T. Robinson, K. Welsher, S. M. Tabakman, S. P. Sherlock, H. Wang, R. Luong and H. Dai, *Nano Res.*, 2010, **3**, 779–793.
21 A. Burke, X. Ding, R. Singh, R. A. Kraft, N. Levipolyachenko, M. N. Rylander, C. Szot, C. Buchanan, J. Whitney and J. Fisher, *Proc. Natl. Acad. Sci. U. S. A.*, 2009, **106**, 12897–12902.
22 C. H. Chou, C. D. Chen and C. R. Wang, *J. Phys. Chem. B*, 2005, **109**, 11135–11138.
23 C. Grabinski, N. Schaeublin, A. Wijaya, H. D'Couto, S. H. Baxamusa, K. Hamad-Schifferli and S. M. Hussain, *ACS Nano*, 2011, **5**, 2870–2879.
24 K. Ke, L. Lin, H. Liang, X. Chen, C. Han, J. Li and H. H. Yang, *Chem. Commun.*, 2015, **51**, 6800–6803.
25 W. Feng, X. Zhou, W. Nie, L. Chen, K. Qiu, Y. Zhang and C. He, *ACS Appl. Mater. Interfaces*, 2015, **7**, 4354–4367.
26 S. Geetha, C. R. Rao, M. Vijayan and D. C. Trivedi, *Anal. Chim. Acta*, 2006, **568**, 119–125.
27 D. Uppalapati, M. Sharma, Z. Aqrawe, F. Coutinho, I. D. Rupenthal, B. J. Boyd, J. Travas-Sejdic and D. Svirskis, *Int. J. Pharm.*, 2018, **543**, 38–45.
28 Y. Yang, B. Gong, Y. Yang, A. J. Xie, Y. Shen and M. Zhu, *J. Mater. Chem. B*, 2018, **6**, 3792–3799.
29 C. Chen, J. Ke, X. E. Zhou, W. Yi, J. S. Brunzelle, J. Li, E. L. Yong, H. E. Xu and K. Melcher, *Nature*, 2013, **500**, 486–489.
30 X. Liu, F. Fu, K. Xu, R. Zou, J. Yang, Q. Wang, Q. Liu, Z. Xiao and J. Hu, *J. Mater. Chem. B*, 2014, **2**, 5358–5367.
31 E. K. Lim, T. Kim, S. Paik, S. Haam, Y. M. Huh and K. Lee, *Chem. Rev.*, 2015, **115**, 327–394.
32 H. Zhang, X. Wang, P. Wang, R. Liu, X. Hou, W. Cao, R. Zhong, X. Liu and Y. Zhang, *RSC Adv.*, 2018, **8**, 37433–37440.

33 X. Hou, X. Wang, R. Liu, H. Zhang, X. Liu and Y. Zhang, *RSC Adv.*, 2017, **7**, 18844–18850.
34 X. Ye, L. Jin, H. Caglayan, J. Chen, G. Xing, C. Zheng, V. Doan-Nguyen, Y. Kang, N. Engheta and C. R. Kagan, *ACS Nano*, 2012, **6**, 2804–2817.
35 D. K. Roper, W. Ahn and M. Hoepfner, *J. Phys. Chem. C*, 2007, **111**, 3636–3641.
36 J. Y. Hong, H. Yoon and J. Jang, *Small*, 2010, **6**, 679–686.
37 G. Das, A. Nicastri, M. L. Coluccio, F. Gentile, P. Candeloro, G. Cojoc, C. Liberale, F. De Angelis and E. Di Fabrizio, *Microsc. Res. Tech.*, 2010, **73**, 991–995.
38 S. J. Yang, F. H. Lin and K. C. Tsai, *Bioconjugate Chem.*, 2010, **21**, 679–689.
39 N. Hao, K. W. Jayawardana, X. Chen and M. Yan, *ACS Appl. Mater. Interfaces*, 2015, **7**, 1040–1045.